Surface modification of oxides by electron-stimulated desorption for growth-mode control of metal films: Experiment and density-functional calculations

T. O. Menteş, A. Locatelli, and L. Aballe*
Sincrotrone Trieste S.C.p.A., Basovizza-Trieste 34012, Italy

A. Pavlovska and E. Bauer
Department of Physics, Arizona State University, Tempe, Arizona 85287-1504, USA

T. Pabisiak and A. Kiejna
Institute of Experimental Physics, University of Wrocław, Plac M. Borna 9, PL-50-204 Wrocław, Poland
(Received 8 March 2007; revised manuscript received 2 August 2007; published 16 October 2007)

Electron-stimulated desorption of bridge-bonded oxygen atoms on the $TiO_2(110)$ surface at elevated temperature is used to produce an oxygen-deficient (1×2) reconstruction. Low energy electron diffraction, x-ray photoelectron spectroscopy, and first-principles calculations show that Au adsorbs on this surface with the substrate periodicity in strongly bonded monomer, dimer, and trimer rows with metallic character. In addition, the experimental evidence combined with the theoretical results points to a missing-row type of structure for the initial (1×2) surface.

DOI: 10.1103/PhysRevB.76.155413 PACS number(s): 68.47.Gh, 68.43.Bc, 68.43.Rs, 68.43.Fg

I. INTRODUCTION

The influence of defects created by electron bombardment on the nucleation and growth of thin films on well-defined halide and oxide surfaces has been known for a long time.[1] The nucleation and growth of Au on LiF(100) is a particularly dramatic example due to the large electron-stimulated desorption (ESD) cross section of F.[2] Most of the early qualitative and the later quantitative work that was concerned with nucleation at defects concentrated on the subsequent growth of three-dimensional (3D) crystals[3–5] and not on low-dimensional (less than three dimensions) growth. On the other hand, one-dimensional metals on insulating substrates are of considerable interest due to their one-dimensional electronic properties and their chemical properties as low-dimensional catalysts. Here, we address specifically the controlled formation of a one-dimensional (1D) metal, Au, using ordered oxygen vacancies created by ESD on a $TiO_2(110)$ surface at elevated temperature. 1D growth of Au on the $TiO_2(110)$ surface can also be induced by photon-stimulated desorption (PSD), which is described elsewhere.[6]

The choice of Au was motivated (i) by the discovery of Haruta *et al.* that Au, which is inert in bulk form, becomes catalytically active in chemical reactions when present in very small clusters ("nanoparticles") on reducible oxides[7] and (ii) by the recent report that Au on CeO_2 is catalytically active not only in the form of nanoparticles but also when distributed as individual ions in CeO_2 particles.[8] The catalytic activity of Au nanoparticles is believed to take place at the perimeter of the particles,[9] with adsorption of some of the reacting species at low coordination sites. In this case, 1D distributions of Au should be particularly catalytically active because of their large perimeter/area ratio and the large number of low coordination sites.

The rutile $TiO_2(110)$ surface (Fig. 1) was chosen because it is known to form a (1×2) structure when oxygen deficient and because of the large number of available complementary experimental and theoretical studies of this surface and its interaction with Au.[10] In the past, the oxygen deficiency was produced by heating to such high temperatures that a significant amount of oxygen was lost from the bulk, causing a high vacancy concentration. Upon subsequent cooling, exchange processes between the surface and the bulk produce a strongly nonstoichiometric surface, which orders in a (1×2) structure.[11] Several models have been proposed for this high temperature (HT) (1×2) structure, mainly on the basis of scanning tunneling microscopy studies: a missing-row structure, in which every second row of bridge-bonded oxygen atoms are removed [12] [Fig. 1(b)] and several added-row structures[13–15] of which the Ti_2O_3 model[13,14] [Fig. 1(d)] is favored. Another recently proposed model[16] is not compatible with detailed low energy electron diffraction (LEED) studies,[17,18] which support the Ti_2O_3 model. First-principles calculations[19] have shown that this added-row structure has a somewhat lower total energy than the missing-row structure

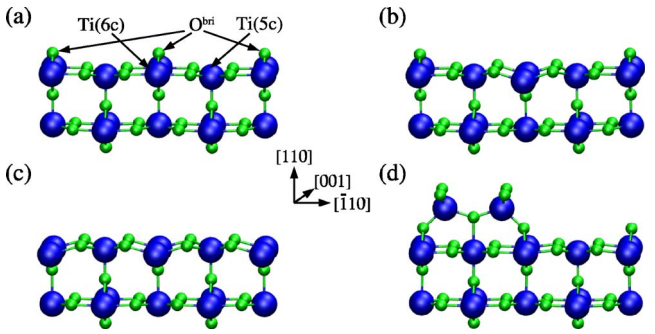

FIG. 1. (Color online) Side view of the TiO_2 rutile (110) surface along the row direction [001]. The large (blue) balls represent the Ti atoms, and the smaller (green) balls the O atoms. (a) The stoichiometric (1×1) structure, (b) (1×2) surface with missing O^{bri} row, (c) reduced surface with all O^{bri} rows removed, and (d) added-row [ar(1×2)] surface.

so that the HT (1×2) structure is generally accepted to have the added-row structure. However, its exact nature is still a matter of discussion.

Here, we demonstrate a different approach, producing a nonstoichiometric (reduced) surface by electron-stimulated desorption of oxygen at temperatures at which no significant oxygen exchange between surface and volume occurs but which are high enough to allow ordering of the surface vacancies. When the oxygen vacancies reach a sufficiently high concentration, the repulsive interactions between them[20] lead to ordering in a (1×2) structure. This low temperature (LT) structure is distinctly different from the HT (1×2) structure, as suggested by the experimental results and verified by density-functional calculations.

The paper is organized as follows. Section II describes the experimental setup. The experimental results are presented in Sec. III. Section IV is devoted to an extended analysis of various Au adatom structures based on first-principles calculations. The results of the experiment are discussed and compared with theory in Sec. V, which is followed by a brief summary (Sec. VI).

II. EXPERIMENT

The experiments were performed in the spectroscopic photoemission and low energy electron microscope at the nanospectroscopy beamline of the synchrotron radiation source Elettra in Trieste, Italy.[21,22] Spatially resolved x-ray photoelectron spectroscopy (XPS) was used for chemical characterization, and very low energy electron microscopy (VLEEM) and LEED for structural characterization. The commercial $TiO_2(110)$ crystals were oriented to within less than 0.5° from the [110] direction. They were cleaned in the preparation chamber by cycles of sputtering for 40 min with 600 eV Ar ions at a current density of about 3 $\mu A/cm^2$, followed by annealing in 5×10^{-6} Torr oxygen at about 860 K for 30 min. After transfer into the main chamber, the surface was inspected by LEED at energies below 33 eV, at which negligible ESD occurs,[23] by mirror electron microscopy (MEM) and by VLEEM. LEED showed a perfect (1×1) pattern. The low energy electron beam in MEM and VLEEM at about 1 eV had no effect on the surface. Electron beam irradiation was performed at a temperature (720 K) which was found to give the best (1×2) structure. The poorer vacancy ordering at lower temperatures is attributed to limited diffusion, and at higher temperatures to oxygen exchange with the bulk. In order to produce various vacancy concentrations in the same experiment, the electron beam spot size on the sample was limited by an aperture to a diameter of 5 μm. The crystal was translated in large enough steps to prevent any interference between regions with different irradiation doses (Fig. 2).

An electron energy of 60 eV was used for electron irradiation. This energy is sufficiently far above the ionization energy of the Ti $3p$ shell (32.6 eV), at which the oxygen ESD cross section rises abruptly,[23] but is small enough so that the dose can be controlled exactly via the irradiation time. With 1 μA emission current (the actual current at the sample is in the nanoampere range but cannot be measured due to the high bias voltage on the sample), 320 s were needed to produce the optimum (1×2) structure. In most experiments, irradiation times were in multiples of 40 s. Under these conditions, we determined a dose error of maximal 2%.

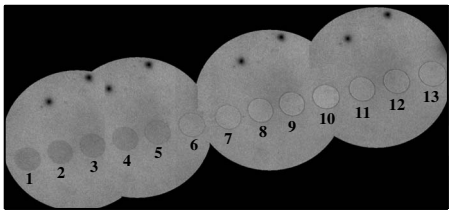

FIG. 2. A series of electron beam irradiated (at 60 eV, and 1 μA emission) spots are imaged close to the MEM-LEEM transition. Spot diameter is 5 μm. The lowest irradiation dose is 40 s and denoted by "1." Each following spot was irradiated in 40 s increments. Spot "8" (320 s irradiation) has the best (1×2) reconstruction. The sample was oriented such that the spot displacement direction coincided with the $[1\bar{1}0]$ direction of the crystal.

The surface structure was characterized by LEED at 31 eV energy (below the Ti $3p$ ionization threshold). No structural change could be observed after bombardment with 0.15 μA emission current for 1 h. Initially, LEED patterns were acquired before Au deposition, but in the course of the study, it turned out that Au deposition had no significant influence on the pattern. In particular, at 0.5 monolayer (ML) vacancy coverage, the LEED patterns were indistinguishable with and without 0.5 ML of Au deposited on the surface. 1 ML of Au at the same vacancy coverage reduced the spot intensities slightly, but also the background in the LEED pattern. Because of these minor differences, in most experiments, Au was deposited at the irradiation temperature immediately after the last irradiation spot was produced in order to exclude possible annealing effects that could influence the vacancy concentration. Au was deposited from an electron bombardment-heated W crucible at a rate of 0.5×10^{-3} ML/s. The rate was calibrated with high accuracy via the time needed to complete 1 Au ML on the W(110) surface. Immediately after Au deposition, the crystal was cooled to about 400 K in order to minimize annealing effects during further measurements. The (1×2) LEED intensity profiles did not change within the first 30 min after Au deposition at about 720 K so that such effects can be safely excluded at 400 K. On the other hand, by keeping the crystal at 400 K, charging of the surface during the measurements was avoided.

For LEED, areas of 2 μm diameter were selected with the illumination aperture. In the XPS experiments, the photon beam was focused to a width of 3 μm. A photon energy of 190 eV was chosen to produce Au $4f$ photoelectrons with a kinetic energy at the minimum of the inelastic mean free path in bulk Au, which is about 0.3 nm at 95 eV.[24] This ensures maximum discrimination between two-dimensional (2D) and 3D growth. Because of the strong photoelectron screening in 3D clusters, the XPS signal from 3D clusters is strongly reduced with respect to that from a 2D layer. The spectra were taken with an energy resolution of 0.3 eV by imaging

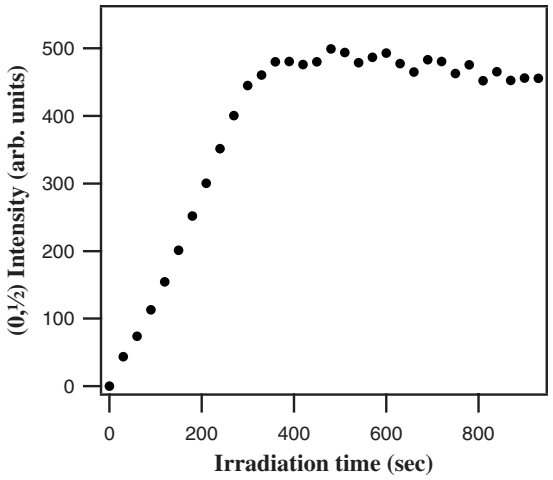

FIG. 3. Intensity of the (0,1/2) LEED spot as a function of electron beam irradiation time at 60 eV electron energy. The LEED patterns were acquired at 60 eV during the irradiation. The optimum (1×2) reconstruction was obtained at about 320 s.

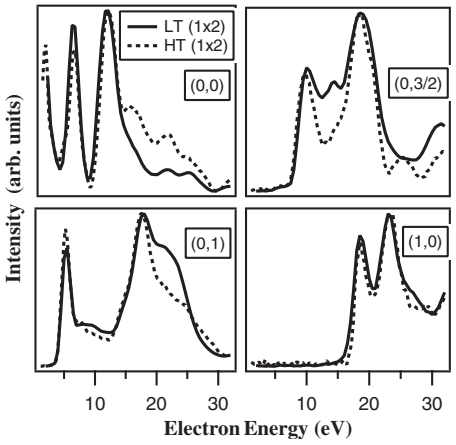

FIG. 4. The LEED $I(V)$ curves for two TiO_2 surfaces showing (1×2) reconstruction. The solid line marked as LT(1×2) is obtained by electron-stimulated desorption (ESD), whereas the dashed curve [HT(1×2) structure] belongs to the surface prepared by high temperature annealing.

with photoelectrons in energy steps of 0.25 eV from 89 to 101 eV with an acquisition time of 4 s per image. This resulted in a spectrum acquisition time of less than 4 min. During the experiments, the pressure was in the low 10^{-10} Torr range except during Au deposition where it rose into the high 10^{-10} Torr range. Between experiments, the surface was cleaned by the sputter-anneal cycles mentioned above. Despite many hours of annealing at 860 K and irradiation followed by Au deposition at 720 K, the crystals showed only a very slight coloration at the end of the study, indicating negligible vacancy creation in the bulk.

III. RESULTS

An array of irradiated regions on which the experiments were performed is shown in the composite VLEEM image of Fig. 2, taken close to the transition between LEEM and MEM. The effect of electron irradiation can be seen in more detail in Fig. 3. It shows the intensity of the LEED (0,1/2) order beam—after subtraction of the background of the unirradiated surface—as a function of irradiation time with 60 eV electrons. Initially, the intensity increases due to a general background increase before the (1×2) structure nucleates and the intensity increases more strongly. This indicates that the vacancies are initially randomly distributed. Subsequently, the half order spot intensity rises rapidly to a maximum at about 320 s irradiation time at which the (1×2) pattern is best developed. This defines a vacancy coverage of 0.5 ML.

After the maximum, the intensity of the half order beams decreases slowly with a constant slope, at least up to 1500 s irradiation time. Simultaneously, the diffraction spots become streaky, indicating the increasing destruction of the (1×2) structure by the desorption of the remaining top layer bridge-bonded oxygen. Simultaneous desorption of second layer bridging oxygen atoms cannot be excluded because they are only 0.39 eV more strongly bound than the first layer bridging oxygen atoms. Desorption of top layer in-plane oxygen atoms appears unlikely because they are much more strongly bound than the bridge-bonded second and third layer atoms.[25,26] Most irradiations were terminated shortly after the maximum because of the unknown surface configuration beyond this point. As shown in Fig. 4, the $I(V)$ LEED curves of the (1×2) structure produced in this manner ["LT(1×2) structure"] are distinctly different from those of the HT(1×2) structure obtained for comparison at the end of the experiments by heating the sample to the high temperatures that produce dark blue coloration. This is a clear indication that the two structures are different.

Figure 5 shows the LEED pattern of the LT(1×2) structure at 0.5 ML vacancy coverage, together with the (1×1) pattern of the surface before irradiation. The increasing intensity and the sharpening of the half order spots with increasing irradiation time is clearly seen in the profiles of the Au-free surface along the $[1\bar{1}0]$ direction (Fig. 6). Upon deposition of Au on the irradiated areas, the (1×2) order is preserved with only slight changes in the spot intensities and the diffuse background. This is in contrast to the unirradiated (1×1) regions, in which the background increases strongly upon Au deposition. This points to the formation of ran-

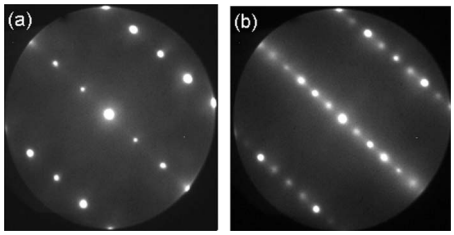

FIG. 5. (a) (1×1) LEED pattern of the TiO_2 surface after a cleaning cycle, and (b) the resulting (1×2) reconstruction after electron-stimulated desorption (ESD) at 60 eV electron energy and 320 s irradiation time. Both images were acquired at 31 eV.

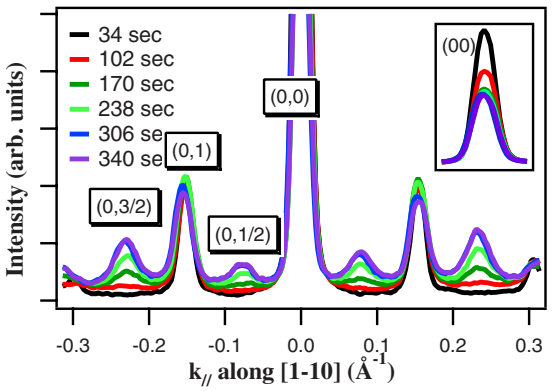

FIG. 6. (Color online) LEED profiles taken along the $[1\bar{1}0]$ direction as a function of electron beam irradiation time. The initial surface shows a (1×1) structure with no trace of the half order peaks. The development of the (1×2) reconstruction with increasing irradiation dose can be seen from the rise in $(0,1/2)$ and $(0,3/2)$ intensities. The decrease in the (0,0) intensity with irradiation time is shown in the inset.

domly distributed Au clusters on the (1×1) surface, and their absence on the (1×2) reconstructed surface. It is also interesting to note that the presence of Au on the irradiated regions does not result in any significant broadening of the LEED spots. Figure 7(a) shows the integrated intensities (after background subtraction) of the (0,0), (0,1), and $(0,3/2)$ LEED spots as function of irradiation time for 1 ML Au deposition. After an initial slow increase, the $(0,3/2)$ spot intensity increases rapidly to a maximum at 320 s while the (0,0) spot shows the opposite behavior. The slow initial increase of the $(0,3/2)$ spot signals a delay of the "nucleation" of the (1×2)-Au structure. There are subtle differences between the evolution of the (1×2) vacancy structure during irradiation and the evolution of the (1×2)-Au structure during Au deposition on the irradiated surface. The nucleation is somewhat delayed, and the intensity decrease after the maximum is faster in the (1×2)-Au layer. This suggests that Au atoms diffuse less easily or tend less to form long chains than vacancies. The full widths at half maximum (FWHMs), which are a measure for the size, shape, and the relative arrangement of the ordered regions, are shown in Fig. 7(b). The width of the half order spots has a minimum at about 320 s irradiation time, corresponding to the best (1×2) structure. On the other hand, the FWHM of the (0,1) spot stays roughly constant until the (1×2) pattern fully develops, and then increases with further irradiation.

The peak shapes of the integral and half order beams of the (1×2)-Au pattern are shown in Fig. 8. The peaks in all LEED patterns were fitted with a combination of a Gaussian and a Lorentzian with peak heights and FWHMs as fit parameters after background subtraction. The background was measured along a line parallel to the profile through the peaks (Fig. 6) at a distance of $2\pi\times0.069$ Å^{-1} from this profile. A fit along the profile $[1\bar{1}0]$ is somewhat ambiguous as the peaks are spaced only $2\pi\times0.077$ Å^{-1} from each other with a considerable overlap of their tails. However, along the [001] direction, the peak spacing is $2\pi\times0.338$ Å^{-1} so that

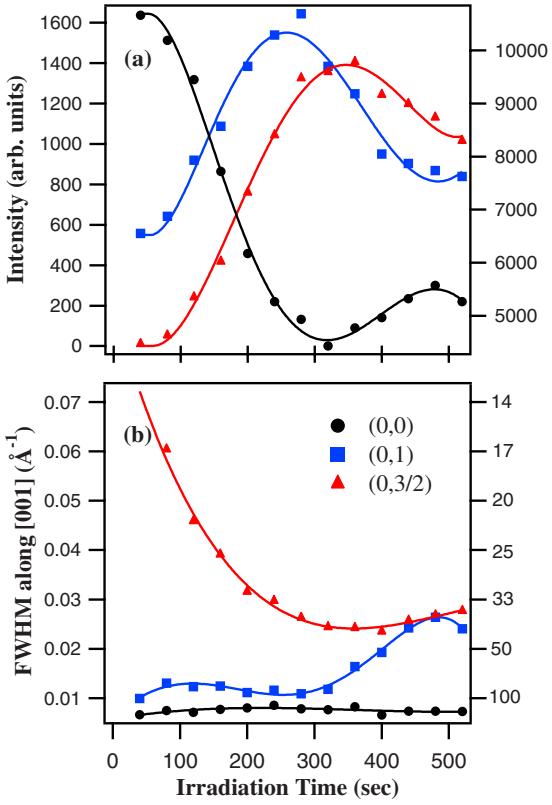

FIG. 7. (Color online) Dependence of the LEED spot intensities and widths on the electron beam irradiation time for 1 ML Au deposition. (a) Intensities of the (0,0), (0,1), and $(0,3/2)$ spots. (b) FWHM values of the same spots obtained from a fit to the peak shape along the [001] direction. The (0,1) and $(0,3/2)$ peaks were fitted with a Lorentzian, whereas the (0,0) peak was a combination of Lorentzian and Gaussian as explained in the text. The figure shows the FWHM of the Gaussian contribution. The corresponding real space length scales are indicated on the right axis in Å. All LEED data are acquired at 31 eV electron energy.

negligible overlap occurs. Along this direction, the (0,1) and $(0,3/2)$ peaks could be fitted well with Lorentzians with FWHMs of $2\pi\times0.012$ and $2\pi\times0.024$ Å^{-1}, respectively. Along the $[1\bar{1}0]$ direction, Gaussian and Lorentzian fits are almost equally good so that a joint fit is rather unstable. Therefore, we chose a pure Lorentzian peak shape for the half order and a pure Gaussian for the integral spots, which give a slightly better fit. The resulting FWHM for the (0,1) peak is equal to its value along the [001] direction within the experimental uncertainty, pointing to a more symmetric shape of the domains whose mean size is approximately 83 Å. On the other hand, the $(0,3/2)$ peak has a FWHM of $2\pi\times0.031$ Å^{-1} along $[1\bar{1}0]$. With the FWHM value along [001] of $2\pi\times0.024$ Å^{-1}, this corresponds to coherent scattering regions of dimensions 42×32 Å^2, elongated along [001].

Contrary to the off-normal beams, the (0,0) peak of the (1×2) pattern clearly gives a better fit with a Gaussian plus Lorentzian [Fig. 8(a)] than with either alone. The Gaussian component may be attributed to the contribution of the bulk, the Lorentzian, which has the same width as the (0,1)

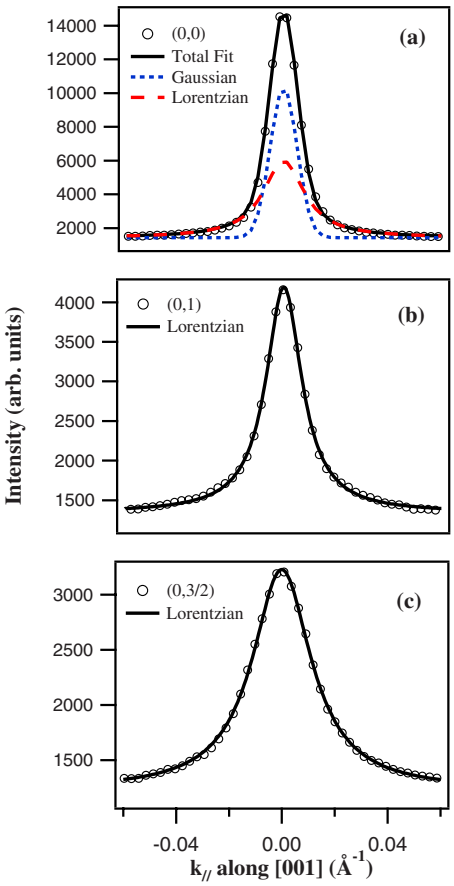

FIG. 8. (Color online) Example fits to the peak shapes of the LEED spots for the (1×2) surface. The three panels show the fits to the (a) (0,0), (b) (0,1), and (c) $(0,3/2)$ spots. The profiles are taken along [001]. The LEED patterns are acquired at 31 eV.

Lorentzian fit, to that of the surface. The (0,0) peak of the (1×1) pattern of the unirradiated surface can be fitted in both directions with a dominant Gaussian with a FWHM of $2\pi\times0.007$ Å^{-1} both in the $[1\bar{1}0]$ and [001] directions. On the other hand, the more surface sensitive (0,1) peak has a larger FWHM of $2\pi\times0.009$ Å^{-1} corresponding to coherently scattering regions with a mean width of 110 Å. This is slightly larger than that of the irradiated surface. In all of the above discussion, the instrumental FWHM, $2\pi\times0.012$ Å^{-1}, is accounted for in the consideration of the LEED spot widths [the instrumental width and the reciprocal space calibration were obtained from a LEED measurement on a virtually step-free region of a W(110) crystal].

The distribution of Au on the surface is strongly influenced by the vacancy density. As an example, Fig. 9 shows the evolution of the Au $4f$ spectrum with irradiation time for a Au coverage of 0.5 ML. The low Au signal on the unirradiated region indicates 3D growth. The intensity increases abruptly from the unirradiated state to the shortest irradiation, corresponding to a transition from 3D crystal growth to a Au distribution in which most Au atoms occupy the oxygen vacancies created by ESD (2D+3D growth). At 0.5 ML vacancies, the growth is purely 2D. The Au $4f_{7/2}$ peak areas are plotted in Fig. 10 as a function of irradiation time for several

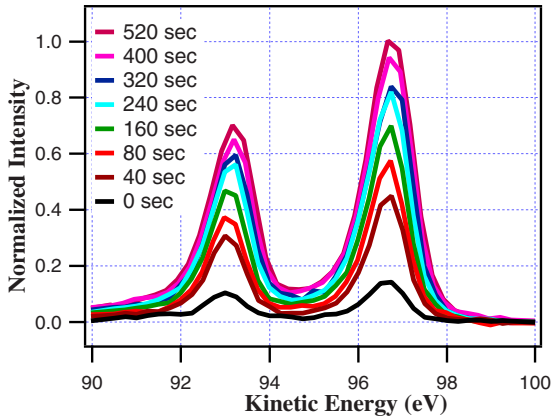

FIG. 9. (Color online) Au $4f$ core level photoemission spectra of a 0.5 ML thick Au film from regions with different electron irradiation times (i.e., with different oxygen vacancy densities, e.g., 0.5 ML at 320 s). The photon energy is 190 eV.

Au coverages. The displayed values were found by a fit using a Doniach-Šunjić function. The spectra were normalized to the linear background of the fit, which has been subtracted in Figs. 9 and 11.

With increasing vacancy concentration, the vacancies organize into the (1×2) structure [Figs. 3 and 5(b)]. The Au atoms form atomic chains in them, and the XPS intensity rises steadily. When the surface is completely covered by the (1×2) structure at about 320 s (dotted line in Fig. 10), the XPS signal levels off but continues to rise afterward again albeit somewhat slower. Note that the kinks in the curves occur at the same irradiation time (and thus vacancy concentration) for the different amounts of Au. The slow rise after 0.5 ML vacancy concentration can be attributed to the electrochemical potential gradient caused by the further oxygen loss for longer electron irradiation, which drives Au diffusion from the surrounding unirradiated regions into the irradiated

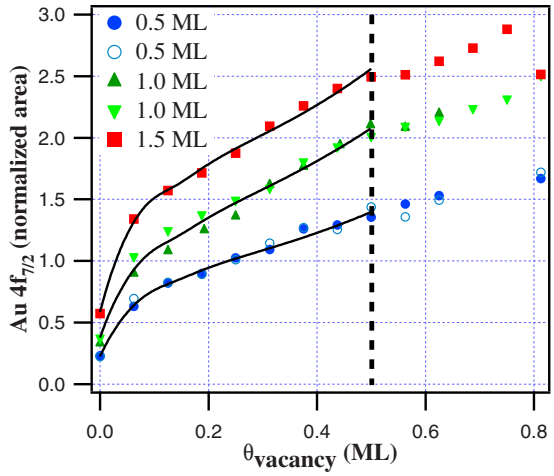

FIG. 10. (Color online) Normalized peak area of the Au $4f_{7/2}$ core level photoemission spectra as a function of irradiation time for three different Au coverages on the TiO_2 surface. The solid lines correspond to the fit as explained in Sec. IV. The dotted line marks the best (1×2) structure.

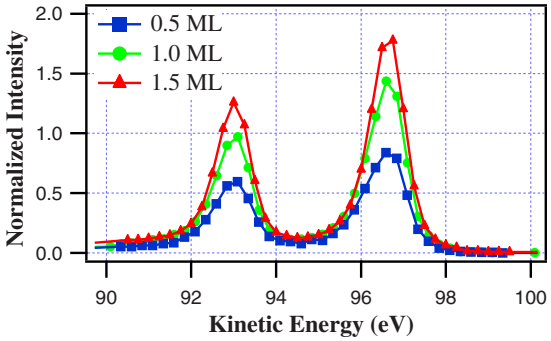

FIG. 11. (Color online) Au 4*f* core level spectra for the three Au coverages on the best (1×2) surface (the dotted line in Fig. 10). In all the spectra, the high kinetic energy base line is normalized to unity and subtracted out.

ones. As already stated in Sec. II, the state of the surface is ill defined for irradiations beyond the completion of the (1×2) vacancy structure, and thus the resulting Au distribution cannot be specified except that it is more or less two dimensional, filling the vacancies in the remaining bridge-bonded oxygen rows and producing a disordered (1×2) structure.

As shown in Fig. 10 on the unirradiated surface, the signal increases only little with Au coverage, mainly due to the increase in cluster size. The clusters, however, are still so small that they cannot be detected by MEM or LEEM, which means that they are smaller than about 10 nm in diameter. As soon as oxygen vacancies are available for Au adsorption, the signal increases significantly with Au coverage. This can be clearly seen in the three spectra for 0.5 ML vacancy coverage [best (1×2) structure, Fig. 11], which indicate that more than one Au row can be incorporated into the (1×2) structure. The position of the peaks does not shift with vacancy density and Au coverage within the limits of error. There is also no clear shift relative to the peaks on the unirradiated regions or, in other words, between 3D Au and lower-dimensional Au.

Finally the following question has to be addressed: How do the electron and photon irradiation used in the measurements influence the results? Figure 12 shows the changes in the LEEM images (a) after the 31 eV LEED and (b) after the XPS measurements. While the trace of the 31 eV irradiation fades out within several hours, that of the 190 eV photon irradiation is permanent. At 31 eV, ESD is negligible as confirmed by the absence of any change in the LEED pattern after extended irradiation at this energy. However, at 190 eV, there is strong PSD, which is evident in the increase of the Au 4*f* photoelectron signal with irradiation time [Fig. 12(c)]. As mentioned before, this increase is attributed to diffusion of Au from the surrounding previously unirradiated regions to the irradiated region, driven by the electrochemical potential gradient due to the additional loss of oxygen. Within the short time required to acquire an XPS spectrum, the influence of the PSD on the Au 4*f* signal is, however, small: In the originally unirradiated regions, no change can be seen, and at 0.5 ML vacancy coverage, the increase is less than 10%.

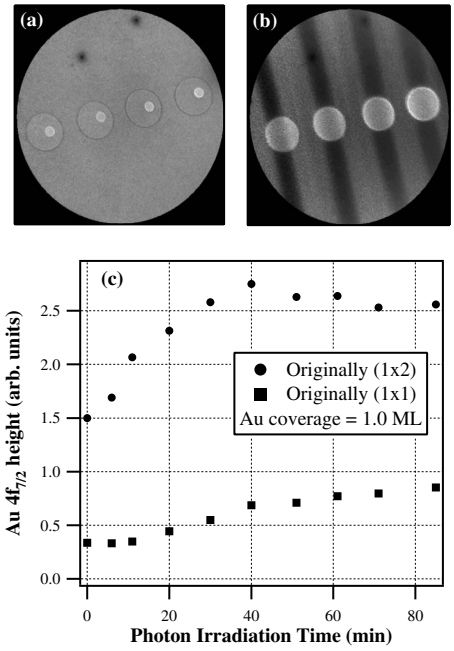

FIG. 12. (a) Effect of the original electron beam irradiation and subsequent LEED measurement as seen by mirror electron microscopy (MEM). The field of view is about 30 μm. The smaller circle inside each irradiated spot is due to the LEED measurement at 31 eV electron energy. (b) Again in MEM mode, one can see the effect of the photon beam used in the XPS measurements as a wide black stripe. The dark contrast is mainly due to photon beam induced reduction of the surface. (c) Effect of extended photon beam irradiation at room temperature on the Au 4*f* signal, outside (squares) and inside (circles) a region electron beam irradiated for 320 s. Au coverage is 1.0 ML. Note that, in the actual experiment, the XPS measurement times were limited to less than 4 min per region.

Up to now, the interpretation of the data in terms of the missing-row structure was based on evidence provided by MEM, VLEEM, and LEED: the fact that the order of the (1×2) structure decreases upon irradiation at temperatures higher than that chosen here and that the $I(V)$ curves are different from those of the added-row structure. Additional evidence is the only slight discoloration of the crystal, indicating no major change of the bulk stoichiometry, which is the prerequisite for the formation of the added-row structure. Qualitative evidences that the Au atoms are forming linear chains in the vacancy rows are the (1×2) structure of the Au-covered surface and the absence of an increase of the background in the LEED pattern. Quantitative evidence could, in principle, be obtained by scanning tunneling microscopy (STM), but the lack of sufficient conductivity of the stoichiometric crystal makes STM difficult. Therefore, we have instead chosen to perform first-principles calculations of the bonding of Au on the $TiO_2(110)$ surface, which provide more information than STM, whose interpretation is not completely unique without theoretical models. The calculations give not only the optimum Au distribution by minimizing the total energy but in addition the binding energy of Au, the exact interatomic distances, the charge distribution,

and the local density of states on the surface atoms. State of the art first-principles calculations are increasingly used as a replacement for the experiments that are difficult to interpret. For this reason, we believe that they will provide the details of the Au distribution on the surface, which cannot be deduced from the experimental methods used here.

IV. THEORY

The density-functional theory (DFT) calculations were carried out using a plane wave basis and projector augmented-wave potentials[27,28] to treat electron-ion-core interactions, as implemented in the VASP code.[29,30] The exchange-correlation energy was calculated within the Perdew-Burke-Ernzerhof version[31] of the generalized gradient approximation. The cutoff energy of the plane wave basis was 400 eV. All calculations accounted for spin polarization. The rutile $TiO_2(110)$ surfaces were simulated by a repeated slab model, in which five TiO_2 trilayers (with 20 Ti and 40 O atoms in a stoichiometric slab) were separated by a vacuum region of 16 Å to avoid spurious interactions between neighboring replicas. Formation of defects, reconstruction of the surface, or adsorption of gold atoms was considered in a (1×2) surface unit cell, symmetrically on both sides of each slab. The corresponding Brillouin zone was sampled by a $1\times4\times1$ Monkhorst-Pack[32] k-point grid with 0.1 eV Gaussian smearing of the Fermi surface discontinuity. The adsorbate and all substrate atoms were fully relaxed in each case until the residual forces on each atom were less than 0.02 eV $Å^{-1}$. We used the optimized lattice parameters of bulk rutile TiO_2 (a=4.669 Å, c=2.976 Å), which were determined in our previous work.[33] The calculated (1×1) structure compares well[33] with experimental data (see also Ref. 34).

The adsorption binding energies have been calculated as

$$E^{ad} = -\frac{(E^{\mathrm{Au}/sub} - E^{sub} - 2NE^{\mathrm{Au}})}{2N}, \quad (1)$$

where $E^{\mathrm{Au}/sub}$ is the total energy of the slab covered with N Au atoms, E^{sub} is that of the Au-free surface slab, E^{Au} is the energy of an isolated Au atom. Both the missing-row [mr(1×2)] and the added-row [ar(1×2)] models were considered. As we have checked, in agreement with a previous calculation,[19] the clean oxygen-deficient ar(1×2) surface is energetically favored over the mr(1×2) structure. The calculated clean ar(1×2) structure is also in overall good agreement with experiment.[17] In addition, the stoichiometric [st(1×1)] surface and the completely reduced [rd(1×1)] surface, in which all bridging O atoms (O^{bri}) are removed, were calculated too.

For adsorption on the stoichiometric (st), missing-row (mr), and reduced (rd) $TiO_2(110)$ surfaces, the Au atoms were placed in the sites depicted in Fig. 13(a): site A in place of the missing O^{bri}; site B (and B') above the Ti($5c$) atom (the prime denotes a symmetric, equivalent site belonging to the same surface unit cell); bridge site C (C') between the atoms of the Ti($5c$) row; site D (D') between the Ti($6c$) and the in-plane O atom; hollow site E (E') between three in-plane Ti atoms; site F between the Ti($5c$) and the O^{bri} atom

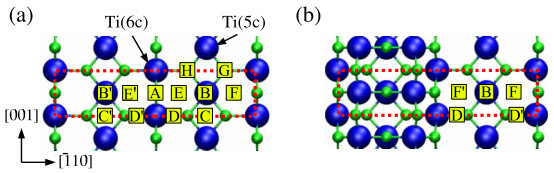

FIG. 13. (Color online) Top view of the (1×2) surface unit cell (marked by dashed line) with labeling of the various initial Au adsorption sites (marked by squares): (a) missing row (1×2) and (b) added row (1×2). Large balls are Ti, and small balls are O atoms.

(equivalent to E' on the rd surface); and site G (H) above the O atom of the basal plane of a TiO_2 trilayer. On the added-row (ar) reconstructed surface, the following initial adsorption sites were considered [Fig. 13(b)]: site B above the Ti($5c$) atom; site D (D') between the Ti($6c$) and the in-plane O atom; and site F (F') between the Ti($5c$) and the O^{bri} atom. The periodic boundary conditions applied ensure that the monomer, dimer, and trimer configurations in the chosen unit cell are not clusters but monomer, dimer, and trimer rows.

The monomer Au row was placed initially in the B sites of the stoichiometric (st) surface and the A sites of the (mr) missing-row and reduced (rd) surface. On the added-row (ar) reconstructed surface, the monomer Au row was placed in the B sites [compare Fig. 13(b)]. The final configurations of the mr and ar surfaces are presented in Fig. 14. After structure optimization, the monomer Au rows adsorb over the initial site A on the mr [Fig. 14(a)] and rd surfaces (not shown) and over the site B on the st (not shown) and ar [Fig. 14(d)] surfaces, without changing their lateral positions during optimization. On the st surface, we have also adsorbed Au atom on top a bridging O atom, which has been reported[35] to be more stable than site B on top a Ti($5c$). In our calculations, the latter site is favored by 0.08 eV, com-

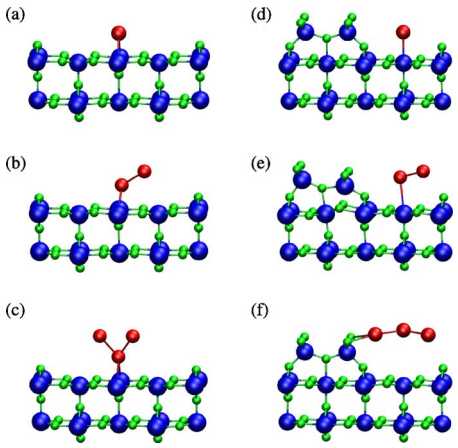

FIG. 14. (Color online) Side views of the final, optimized configurations of the monomer, dimer, and trimer Au rows adsorbed on the missing-row surface (left column) and the added-row reconstructed surface (right column). Large (blue), medium (red), and small (green) sized balls represent Ti, Au, and O atoms, respectively.

TABLE I. The adsorption energy per atom E_{ad} and the Au-Ti and the Au-Au bond lengths of the various Au row configurations on the stoichiometric (st), missing-row (mr), added-row (ar) and reduced (rd) $TiO_2(110)$ surfaces shown in Fig. 14. Note that the *AD* and *DAD′* indicate the initial adsorption sites. The optimized Au positions can be seen in Fig. 14. For trimer rows, the given Au-Au distance is between the central Au and each of the side atoms.

Structure		E_{ad} (eV)	$d_{\text{Au-Ti}}$ (Å)	$d_{\text{Au-Au}}$ (Å)
Monomer	st *A*	1.35	2.51 (Au-O^{bri})	
	st *B*	1.43	3.03	
	mr *A*	2.83	2.67	
	rd *A*	2.99	2.67	
	ar *B*	1.56	2.68	
Dimer	mr *AD*	2.51	2.73	2.78
	ar *BD′*	2.06	3.19	2.69
Trimer	mr *DAD′*	2.42	2.78	2.85
	rd *DAD′*	2.51	2.75	2.85
	ar *DBD′*	2.25	4.78	2.70

pared to that on top of O^{bri}. The respective adsorption energies and the Au-Ti bond lengths are presented in Table I. Adsorption on the rd surface (not shown) gives a configuration very similar to that on the mr surface, with an increased corrugation of the surface plane.

For the dimer row adsorption, the following initial site combinations were considered: *AB*, *AC*, *EE′*, *DD′*, *EF*, and *GH*, on the mr surface, and *BD′*, *BF*, and *FF′* sites on the ar surface. The most stable structures resulted for Au initially in *AC* sites on the mr surface [Fig. 14(b)] and in *BD′* sites on the ar surface [Fig. 14(e)]. Note that during optimization, the Au atoms on the mr surface shift from the initial *AC* configuration substantially toward each other in the $[1\bar{1}0]$ direction [Fig. 14(b)]. The Au atom initially on site *C* shifts toward site *D* by 1.08 Å and is distant from site *D* only by 0.21 Å. Also, the Au atom initially on site *A* shifts laterally toward site *D* by 0.28 Å. Consequently, the resulting configuration is closer to *AD* than *AC*. The initial *AD* configuration was not considered because as judged by our experience with trimer rows (see below), we suspect that it ends exactly in the same configuration as that resulting from the *AC* initial configuration.

A closer analysis of the energetics of the top atom in the *AD* dimer shows that the top Au atom may oscillate between the two *D* positions—right and left of the bottom atom. We have checked this possibility by putting the top atom in some positions along the line between the optimized position [see Fig. 14(b)] and the position above the first Au atom and allowing it to relax only vertically at the frozen configuration of other atoms (substrate and the other Au). The second Au in those intermediate top positions gives the same binding energy (within 5 meV), and the same Au-Au distance, as for Au in the optimized position *D*. When the structure (including the bottom atom) is fully relaxed, the binding energy for the second atom on top of the lower Au and in intermediate positions between the top position and the optimized position *D* is slightly higher (by ≅10 meV) than in *D*. This is still within the accuracy of our calculations, so we estimate that at the temperature at which our XPS measurements are done, the top Au atom will oscillate between the two *D* positions.

In the asymmetric dimer row on the ar surface, the Au atoms shift from the initial sites *B* and *D′* further apart from each other by 0.24 and 0.27 Å in the $[1\bar{1}0]$ direction. Note that this asymmetric dimer configuration causes also an asymmetric shift of the added-row atoms [Fig. 14(e)].

Trimer Au rows on the mr and rd surfaces were initially arranged as *BAB′*, *CAC′*, *DAD′*, and *EAE′*. On both surfaces, the same most stable optimized structure results from the initial *CAC′* or *DAD′* configurations. The Au atoms move from the *C*(*C′*) and *D*(*D′*) positions in the $[1\bar{1}0]$ direction to positions which are 0.6 Å away from the central Au row, i.e., closer to it than in the initial *C*,*D* and *C*,*D′* sites, as shown for mr surface in Fig. 14(c). They also shift a large distance (≅4.4 Å) away from the surface forming together with the central Au atom (over site *A*) a three-dimensional Au stripe [compare Fig. 14(c)]. The distance between the top atoms of the trimer on the mr surface is 2.79 Å and slightly larger (2.83 Å) on the rd surface.

On the added-row (ar) reconstructed surface, the initial site configurations *DBD′* and *FBF′* were considered. The structure resulting from configuration *DBD′* appeared to be favored [Fig. 14(f)]. The Au atoms in the resulting structure are shifted a large distance away from the surface plane (4.71 and 4.53 Å for sites *B* and *D*, respectively). This explains the substantial outward shift of the added-row atoms (0.05 Å for Ti and 0.03–0.09 Å for O), because they form bonds with the Au atoms in *D* and *D′* (Fig. 14). The distance between the outer Au atoms in the *DBD′* trimer is 4.50 Å.

No shift of the Au atoms in the [001] direction is observed for all configurations studied, i.e., they are in registry with the substrate atoms. A comparison of the adsorption energies between mr and ar surfaces in Table I shows that they decrease with the number of atoms on the mr surface while they increase with the number of atoms on the ar surface. This can be understood easily because each additional atom adds to the total adsorption energy an amount of the order of the binding energy of the diatomic Au molecule, 2.3 eV.[36] As a consequence, the average adsorption energy decreases on the mr surface where the monomer binding energy is higher than 2.3 eV, while it increases on the ar surface where the binding energy of the monomer is lower.

The electron density charge redistribution in the adsorption system is given by the difference in electron-charge densities of the complete adsorption system and the sum of the bare substrate, and the free adsorbate (Au) at the positions of the relaxed Au/TiO_2 system. The isosurfaces of the difference charge distribution for the mr and ar surfaces are plotted in Figs. 15 and 16, respectively. Positive values of the isocharge surfaces show regions with electron-charge gain upon Au bonding. As it is seen, the electron-charge gain distribution differs distinctly between the two surfaces. In the case of monomer, dimer, or trimer row adsorption on the mr surface, a stripe of accumulated one-dimensional electron gas extends between the Au and Ti atoms along the Au rows in the [001]

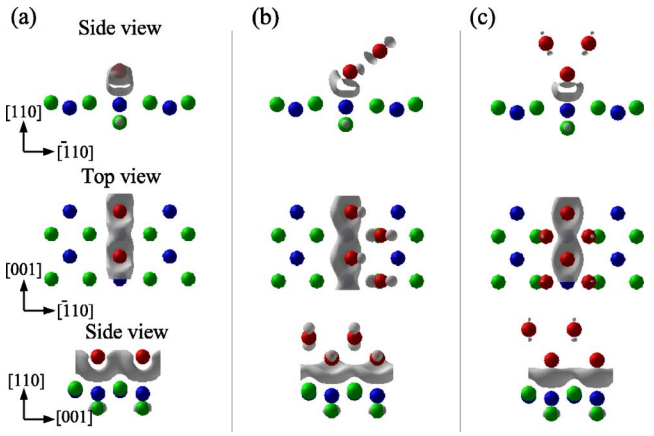

FIG. 15. (Color online) Electron density charge gain upon Au adsorption on the mr surface. Blue, green, and red balls represent Ti, O, and Au atoms, respectively. Isocharge surfaces in all graphs correspond to 0.03 electron/Å^3. The configurations shown in columns (a)–(c) correspond to the monomer, dimer, and trimer Au rows displayed in Figs. 14(a)–14(c).

direction. In the monomer, Au row on the ar reconstructed surface such an electron-charge stripe is also visible. However, the plotted isocharge value on the ar surface is only 1/3 of that on the mr surface.

In order to quantify the valence electron-charge transfer to and/or from adsorbed Au atoms, we have calculated the charge included in a sphere of radius R_{Au}, around both a free (isolated) and adsorbed Au atom, and their difference per sphere, for the various adsorption configurations. The amount of charge enclosed in the sphere, which is presented in Table II, gives a rough estimate of the charge loss or gain in a given configuration. The overall amount of charge around Au changes only negligibly upon adsorption on the stoichiometric surface, thus reflecting the weak Au binding

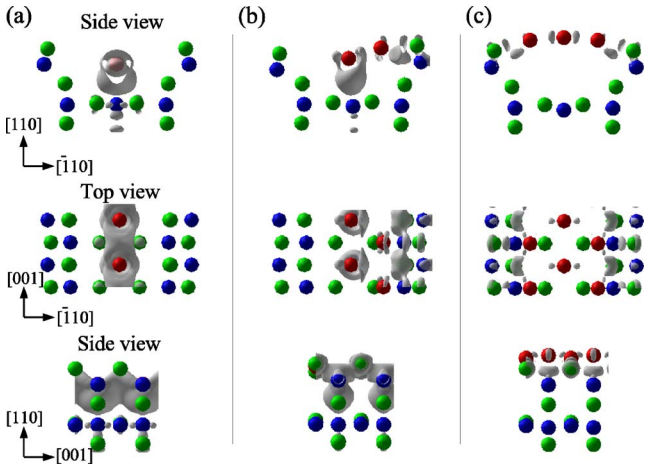

FIG. 16. (Color online) Electron density charge gain upon Au adsorption on the ar surface. Blue, green, and red balls represent Ti, O, and Au atoms, respectively. Isocharge surfaces in all graphs correspond to 0.01 electron/Å^3. The structures shown in columns (a)–(c) correspond to the monomer, dimer, and trimer Au rows presented in Figs. 14(d)–14(f).

in this configuration. In general, on the mr and rd surfaces, the amount of charge gain around the Au atom decreases with the number of atoms that form the row and follows the weakening of the adsorption energy per atom (compare Table I). The charge gain of the bottom Au atoms on the mr surface is mainly of the *sp* type and is due to charge transfer in part from the Au *d* states and in part from the more electropositive Ti atoms. The smaller charge gain on the ar surface is reflected in the weaker bonding to the substrate.

A point worth mentioning is related to the Au 4*f* core level shifts for the different configurations considered. The last column in Table II shows the calculated values with respect to the bulk Au, including final state screening effects. Not shown in the table is the result for the surface core level shift for the Au(111) surface, which is calculated to be −0.28 eV. This is in good agreement with the experimental value of −0.4 eV.[37] Considering the surface sensitivity of the photoemission measurements described in the previous section, the surface core level is a more appropriate reference for the comparison between the different 2D distributions and the 3D crystallites of Au. Accordingly, one can observe that the core level shifts of 3D crystallites and monomer rows do not differ significantly.

V. DISCUSSION

The results described in Sec. III clearly show that the surface damage caused by sputtering and electron and photon irradiation can be eliminated, at least on the 10 nm scale, by annealing in oxygen at temperatures at which no noticeable change of the bulk stoichiometry occurs. The high peak-to-background ratio in the LEED pattern is an indication of high crystal perfection, albeit limited in range. As judged by the shape and half-width of the diffraction peaks, the domain size has a wide distribution with an average width of about 110 Å. Since no extended defects, which could cause lateral shifts in the crystal lattice, can occur at the temperatures used here, the limited domain size is attributed to local height differences on the surface of the crystal. These are a natural consequence of the limited surface diffusion range at the annealing temperature.

Electron-stimulated desorption of oxygen during irradiation at elevated temperature produces a lateral surface mass transport leading to the formation of the (1×2) structure. In this structure, regions which are displaced laterally by one-half of the double periodicity can form in different regions on the surface. At the low irradiation temperature and short irradiation times, surface diffusion is further limited so that these regions are smaller than the domains on the (1×1) surface as evident from the shorter coherence length observed. The nucleation and growth of the (1×2) domains at lower vacancy coverages can be seen in the evolution of the 1/2 order spots with coverage. At higher vacancy coverages, the creation of vacancies in the second set of bridge-bonded oxygen rows disorders the surface again.

The surface that the arriving Au atoms see may thus be visualized as rough on the nanometer scale with mean lateral dimensions of several nanometers but atomically flat on the atomic scale. At 0.5 ML vacancy coverage, these regions

TABLE II. The amount of *l*-decomposed valence charge calculated in a sphere of radius R_{Au}=1.50 Å around the Au atom adsorbed on stoichiometric, missing-row, and added-row (1×2) reconstructed $TiO_2(110)$ surfaces with respect to the free atom. Units are electron per sphere. The CLS column displays the calculated shifts of Au 4*f* core level in the Au atom belonging to the monomer, dimer, or trimer row structure on the $TiO_2(110)$ surface. The shifts are calculated with reference to the bulk Au value (−23.716 eV).

Structure		Au atom	Electron charge				CLS (eV)
			s	*p*	*d*	Total	
Monomer	st *A*		−0.004	0.034	−0.022	0.008	−0.216
	st *B*		0.022	0.014	−0.034	0.003	0.278
	mr *A*		0.308	0.120	−0.207	0.221	−0.412
	rd *A*		0.312	0.122	−0.210	0.224	−0.344
	ar *B*		0.186	0.066	−0.144	0.107	−0.796
Dimer	mr *AD*	Bottom	0.187	0.110	−0.138	0.159	−0.634
		Top	0.050	−0.005	0.002	0.039	−1.618
	ar *BD′*	Bottom	0.081	0.013	−0.041	0.033	−0.451
		Top	−0.003	0.078	−0.034	0.041	−0.398
Trimer	mr *DAD′*	Bottom	0.161	0.121	−0.131	0.150	−0.728
		Top	0.020	−0.008	0.012	0.024	−1.663
	rd *DAD′*	Bottom	0.182	0.132	−0.151	0.162	−0.517
		Top	0.021	−0.006	0.012	0.027	−1.724
	ar *DBD′*	Bottom	0.008	0.052	−0.036	0.023	−1.165
		Top	0.015	0.015	−0.015	0.016	−1.576

contain one to several domains of the (1×2) structure with vacancy rows. At vacancy coverages below 0.5 ML, the (1×2) structure domains are smaller and surrounded by (1×1) regions, while above 0.5 ML, the (1×2) structure is degraded by desorption of oxygen atoms in the remaining bridge-bonded rows on the surface and possibly below the surface.

At the atomic level, the (1×2) structure created by ESD at 720 K is clearly different from the one obtained by high temperature annealing. The LEEM study by McCarty and Bartelt[11] shows convincingly that the formation of the HT(1×2) structure requires a high bulk defect density (Ti interstitials and O vacancies) and that considerable mass flow, both of Ti and O, occurs during the transition from the (1×1) structure at high temperature to the HT(1×2) structure upon cooling. The frequently cited result by Henderson[38] that Ti cations and not O ions or vacancies are the major diffusing species is not in disagreement with the LEEM work,[11] because Henderson studied crystals whose surface was Ti enriched by preferential sputtering of oxygen. This produces a chemical potential gradient enhancing Ti cation diffusion.

In our case, the only slight discoloration of the crystal after many heating cycles clearly indicates that the bulk defect concentration is negligible. Therefore, no significant mass transport between surface and the bulk can occur, which would be necessary in the formation of the added-row HT(1×2) structure. Rather surface diffusion must be responsible for the observed LT(1×2) structure. With the surface Ti cations strongly bound to the surrounding O anions, the obvious diffusing species is O (whether one wants to call it O vacancy or O atom diffusion is a semantic question because the movement of an O atom to a neighboring O vacancy is equivalent to the movement of an O vacancy in the opposite direction).

Thus, there is a fundamental difference between the processes leading to the formation of the HT(1×2) and the LT(1×2) structure. In the former, it is the different temperature-dependent concentrations and diffusivities of Ti interstitials and O vacancies in a highly defected crystal which lead to a (1×2) structure upon cooling; in the latter, it is the O desorption, O surface diffusion, and the repulsive interaction between vacancies that produce a (1×2) structure at constant temperature without involving bulk diffusion.

The difference between the two (1×2) structures is evident in the LEED $I(V)$ curves shown in Fig. 4. There is ample evidence from STM studies that the HT(1×2) phase has the added-row structure. The formation process of the LT(1×2) structure, which only involves removal of bridge-bonded O atoms, surface vacancy diffusion, and ordering, does not allow the more massive reconstruction seen in the added-row structure and leaves only the missing row structure for interpretation. That the mr(1×2) structure has a somewhat higher energy than the ar(1×2) structure[19] is no argument against this interpretation because the mr(1×2) structure is clearly a kinetically limited structure for lack of material exchange with the bulk. Indeed, upon electron beam irradiation at temperatures higher than 720 K, we obtained a much poorer (1×2) order, probably due to material exchange with the bulk.[11]

There is still a possible objection to this interpretation that has to be addressed. The calculations of vacancy interactions[20] predict that $c(n\times 2)$ configurations have lower energies than $(n\times 1)$ configurations $(n=2-6)$ corresponding to vacancy coverages from 0.5 to 0.17 ML. No calculations were made for mr(1×2) structure segments with corresponding coverages. Therefore, these calculations do not contradict our experiment, in which not the slightest indication of ordering in a $c(n\times 2)$ or $(n\times 1)$ structure could be seen at any vacancy coverage. It should be noted that there are many adsorption systems in which repulsive lateral interactions do not produce structures that maximize interatomic distance but rather close-packed rows, in particular, on substrates with close-packed rows.

On the other hand, independent of the discussion on whether the surface reconstruction is added row or missing row, the XPS and LEED results lead to the conclusion that Au is distributed in rows on the LT(1×2) surface. The large XPS Au $4f$ signal in the (1×2) regions compared to that on the (1×1) regions shows that the distribution is either one or two dimensional. The excellent (1×2)-Au LEED pattern and the lack of an increase in the background compared to the LEED pattern before Au deposition indicate that the distribution is 1D. As far as the distribution of Au in the rows is concerned, LEED allows only the conclusion that the Au distances are the same as in the substrate: 13 Å between the chains and 2.95 Å along the chains, which is only 2.3% larger than the interatomic distance in bulk Au. Not much more can be deduced from experiment about the Au distribution except from the observation that the Au $4f$ XPS signals in Fig. 11 are not proportional to the Au coverage. This suggests photoelectron absorption due to outward growth. Unless counteracting effects occur, the lack of a clear chemical shift of the Au $4f$ signal shows that Au is essentially metallic. The largely metallic nature of the Au atoms and their nearly identical interatomic distances as in the bulk indicate metallic conductivity along the rows.

The experimental evidence that the Au is distributed in one-dimensional chains has to be considered in light of the DFT calculations. As explained in Sec. IV, the calculations show that the Au chains are strongly bound to oxygen-deficient surfaces. In particular, the results summarized in Table I demonstrate clearly that the binding of Au chains is considerably stronger to the missing row in comparison to the added row reconstructed (1×2) surface. Combining this with the preceding discussion on the differences between the LT(1×2) and HT(1×2) structures, we strongly believe that the ESD generated LT(1×2) surface has a missing-row-type reconstruction.

Much more detailed information can be drawn from the first-principles calculations. First of all, they show that the linear Au distribution is strongly bound, thus favoring chain formation, that there is little charge transfer between Au and the substrate, and that there is a noticeable density of states at the Fermi level, indicating metallic conductivity, in agreement with experiment. Far beyond the experiment, the calculations give detailed information on atomic positions, charge distribution, and, in particular, the location of the Au atoms above the oxygen vacancy. Contrary to simple expectations, the additional atoms rather attach to the first atoms mostly in the outward direction. The small differences in the binding energies of the top atom of the dimer row on the mr surface between the position shown in Fig. 14(a) and on top of the bottom atom suggest that the top atom is oscillating about the bottom atom between left and right. This will cause some shielding of the photoelectrons emitted from the bottom atom. Similarly, the top atoms of the trimer attenuate the photoelectronemission from the bottom atom. The attenuation necessary to explain the less than proportional increase of the Au $4f$ intensity with number of atoms per row is larger than in the bulk. This is not surprising because the energy losses in the "molecular" rows are certainly different from those in the bulk. Furthermore, photoelectron diffraction can reduce the forward emission measured in this experiment considerably. It is interesting to compare the trimer row configuration with that of the ten-atom Au cluster[39] attached to a group of three neighboring vacancies along the [001] direction. The Au atoms closest to the surface have a configuration similar to that of our trimer group. This suggests that rows with more than three atoms per unit cell may be formed, as expected also from experiment though not tested.

A very recent study combining STM and first-principles calculations has demonstrated that at room temperature, Au atoms tend to bind to single oxygen bridging vacancies on a slightly reduced surface.[40] The calculations show that the binding energies of Au clusters to single vacancies are significantly smaller than the binding energies calculated here for vacancy rows. The larger values obtained here are due to the additional Au-Au bonding along the rows as seen in Figs. 15 and 16.

Obviously, the dependence of the Au $4f$ signal intensity on vacancy coverage θ (shown in Fig. 10) cannot be described by a simple expression $I=I_c(1-\theta)+I_m\theta$, where I_c is the signal from the 3D Au crystallites in the unirradiated region and I_m that from the m-mer Au rows (meaning m atoms per oxygen vacancy) at the optimum (1×2) structure. It has to be kept in mind that initially, only randomly distributed vacancies exist, as evidenced by the delayed rise in the half order spots in Fig. 7(a). Due to repulsive lateral interactions, they arrange into row segments with increasing vacancy coverage until the surface is completely covered with (1×2) vacancy rows. If the number of Au atoms is larger than the number of vacancies, each vacancy or vacancy row segment will bind several Au atoms. For example, for 1.0 ML Au, each vacancy will bind on average n Au atoms at $\theta=1/n$. Initially, the number of these Au clusters increases proportionally to the number of vacancies but it subsequently decreases rapidly with increasing length of the vacancy row segments once they form. These can accommodate Au atoms in Au m-mer rows that are energetically more favorable as shown in Sec. IV. Obviously, the signal per Au atom in the n-atom clusters is lower than that from n 2D-distributed atoms due to attenuation by inelastic scattering within the clusters. If the average signal from these clusters is called I_n, then the evolution of the Au $4f$ signal per Au atom with vacancy coverage may be expressed in a highly simplified form by

TABLE III. I_c, I_n, and I_m values obtained form the fit of Eq. (2) to the experimental data shown in Fig. 10. θ_0 was determined as 0.15 ± 0.03 from an initial fit to all the data. This value was fixed in a subsequent fit giving the results listed in the table.

Au coverage (ML)	I_c	I_n	I_m
0.5	0.24±0.04	0.47±0.03	1.28±0.03
1.0	0.38±0.04	0.63±0.10	1.86±0.06
1.5	0.59±0.04	0.92±0.03	2.29±0.04

$$I = I_c\left(1 - \frac{\theta}{\theta_0}\right) + I_n\frac{\theta}{\theta_0}e^{(1-\theta/\theta_0)} + 2I_m\theta, \tag{2}$$

where θ_0 is the vacancy coverage at which the coverage of the n-atom Au cluster is largest. As mentioned earlier, and I_c, I_n, and I_m represent the signals per Au atom for 3D crystallites, n-atom clusters, and m-mer rows ($m=1,2,3$), respectively. The first term on the right, which is the contribution of the crystallites, is set to zero for ($\theta > \theta_0$). The factor of 2 in the last term is used in order to normalize θ to the vacancy coverage at the complete (1×2). The fit of this expression to the experimental data (solid lines in Fig. 10) gives the I_c, I_n, I_m, and θ_0 values shown in Table III. (Notice that the numbers listed in the table have to be considered in arbitrary units, as they contain a constant factor depending on the photoionization cross section and the normalization, among other things. This factor is irrelevant for our discussion, in which we consider only the ratios.) The average I_n/I_m ratio is 0.36 ± 0.04 for all Au coverages shown in this figure. This does not mean that all clusters have the same size because I_m increases from monomer to dimer to trimer row as 1.0:1.47:1.79. Apparently, the photoelectron attenuation in molecules is stronger than in the bulk. The I_n values of 0.47, 0.63, and 0.92 for Au coverages of 0.5, 1, and 1.5 ML correspond to increasing cluster sizes.

Information about the Au crystallites in the unirradiated areas can be obtained from the ratio I_c/I_0 derived from the experiment, where I_0 is the signal from a single Au atom. In order to do this, assumptions of the crystallite shape and size have to be made. This can be done on the basis of several experimental[35,41–45] and theoretical[42,46–48] studies of Au clusters and crystallites on the $TiO_2(1\times1)$ surface. While the theoretical studies apply mostly to small clusters which may be expected in the irradiated regions at low vacancy density, the experimental work addresses primarily the larger clusters and small crystallites. Depending on Au coverage and deposition or annealing temperature, the particle shapes range from more or less hemispherical to nearly spherical shape, the latter with reduced contact area with the substrate. Under our experimental conditions, mostly spherical crystallites are expected but hemispherical ones cannot be excluded. For simplicity, we consider cylindrical crystallites with radius r and height h, which contain the same number of atoms as spherical and hemispherical crystals with the same radius, corresponding to height $h=4/3r$ and $2/3r$, respectively. As an average, we choose $h=r$. In a cylindrical crystallite consisting of n (111) layers and containing N atoms, $N=2.42n^3$ for the lattice parameters of Au. The number of atoms in the topmost layer is then N/n and the Au $4f$ signal from each crystallite is

$$I_{c1} = \left(\frac{N}{n}\right)\frac{[1-e^{-nh_0/\lambda}]}{[1-e^{-h_0/\lambda}]}, \tag{3}$$

where $\lambda \cong 0.3$ nm is the inelastic mean free path of 90 eV electrons in Au and h_0 the interlayer spacing. Because of the small value of λ, the signal from a five layer thick crystallite which contains about 300 atoms differs by only 2% from that of an infinitely thick crystal, $1.84I_0N/n=2.47I_0N^{2/3}$, where I_0 is the unattenuated signal from a single Au atom. As judged by published data,[44–49] our crystallites contain at least 300 atoms so that all crystallites will contribute about this value to the measured Au $4f$ signal from the unirradiated regions, I_c. Then, $I_c=2.47N_cI_0N^{2/3}$, where N_c is the number of crystallites in the sampled area A. This value has now to be compared with that from the complete (1×2)-Au row structures with monomer, dimer, and trimer Au rows, I_m. As Table III shows, the ratio I_c/I_m is 0.20 for $\theta_{Au}=0.5$ and $\theta_{Au}=1.0$ within the limits of error and is 0.26 for $\theta_{Au}=1.5$. Taking attenuation into account, $I_1=I_0N_0$, $I_2=1.47I_0N_0$, and $I_3=1.79I_0N_0$, where N_0 is the number of adsorption sites in the (1×2) structure within the sampled area. This leads to $N_cN^{2/3}/N_0$ values of 0.08, 0.12, and 0.19 for the three Au coverages. Because of the high Au deposition temperature at which considerable Au diffusion occurs, it is unlikely that the increase of $N_cN^{2/3}/N_0$ is due to an increase of N_c. It is rather caused by the growth of the crystallites, approximately proportional to their surface ($\sim N^{2/3}$). The crystallite coverage $(N_c/A)/(N_0/A)=N_c/N_0$ can be estimated by assuming a few N values. For the lowest Au coverage and $N=300$ and 1000, N_c/N_0 is 1.8×10^{-3} and 8×10^{-4}, respectively. The corresponding crystallites have heights of about 12 and 18 Å. Their diameters are about 24 and 35 Å, well below the resolution limit of the instrument.

The increase of the Au $4f_{7/2}$ signal upon electron irradiation beyond the optimum (1×2) structure (Fig. 10) and upon extended photon irradiation [Fig. 12(c)] has been attributed to Au diffusion from the unirradiated region into the irradiated region. It occurs without noticeable decrease of the Au signal in the unirradiated region. This can be explained as follows. In the unirradiated region, Au is present in large clusters which contribute little to the Au signal per atom. When the Au atoms in these clusters are incorporated into the Au rows of the (1×2) structure, the signal per atom increases markedly due to the weaker attenuation. The large clusters wet the unirradiated surface poorly and are mobile. Cluster mobility has long been invoked in order to explain the number density of 3D crystallites in thin film growth (see, for example, Refs. 35–45 in Ref. 49). Cluster diffusion has also been observed by STM in Au films on the $TiO_2(110)$-(1×1) surface for clusters smaller than 50 Å in diameter, mostly along the [001] (row) direction.[44] Recent molecular dynamics simulations with parameters obtained from first-principles calculations of Pd on MgO(100) have

shown that small clusters indeed diffuse faster than individual adatoms.[50]

The results of this and of a previous study[6] illustrate the power of ESD and PSD for the control of the growth of Au on TiO_2(110) surfaces and probably also on other reducible oxide surfaces. This power is not limited to such surfaces but is also very effective in ionic crystals, as already shown in the early work for alkali halides and fluorides.[2,51] In these compounds, the electronegative species is desorbed with high efficiency, predominantly via interatomic Auger transitions from core holes in the electropositive species but also via intra-atomic Auger transitions from core holes in the electronegative species.[52–54] The high ESD cross section of halogens should be useful for the study of the influence of Cl and other adsorbates resulting from the technical catalyst preparation procedures on catalytic properties. Thus, ESD and PSD are useful not only for the control of the catalyst distribution in model studies but also for the study of the influence of technological preparation procedures. This makes ESD and PSD an important tool in the efforts aimed at the fundamental understanding of oxide supported catalysis by metals.

VI. SUMMARY

Electron and photon-stimulated desorption of oxygen surface atoms at moderate temperatures has been shown to produce ordering of the resulting vacancies into vacancy rows on the TiO_2(110) surface, thanks to the mobility of the vacancies and the repulsive interactions between them. The resulting missing-row (1×2) surface acts as template for the formation of ordered Au atom rows of up to three or more Au atoms per row unit cell. With increasing Au coverage, sequentially, monomer, dimer, and trimer rows are formed. From a detailed LEED profile analysis, mean dimensions of the coherently scattering regions of about 60 Å are obtained. First-principles calculations give a detailed picture of the structure, bonding and electronic configurations of the Au rows. In particular, they reveal the strong bonding to the substrate and the metallic nature of the rows. The controllable number of atoms per row should be useful for the study of the catalytic behavior of Au on TiO_2.

ACKNOWLEDGMENTS

A.P. and E.B. acknowledge support by the National Science Foundation under Project No. 00315412. The work of T.P. was supported by the Polish Ministry of Science in the year 2007 within the Research Project No. N202 005 32/0469.

APPENDIX: ON THE EFFECTS OF ELECTRON BOMBARDMENT

It has been pointed out that electron bombardment can change the surface significantly, beyond the simple loss of bridging oxygen atoms as shown in a recent cursory STM study.[55] In this work, the TiO_2 surface was bombarded at room temperature with 75 and 300 eV electrons. The former, low energy irradiation was shown to create oxygen vacancies [which start clustering into (1×2) strands above 12%] along with isolated pits. The higher energy, 300 eV, irradiation resulted in a mixture of nanoscale (1×2), (1×3), (1×4), and (1×5) domains. In LEED, these configurations would produce a (1×1) pattern with a strong background. This is, indeed, what we found in our systematic studies as a function of irradiation and annealing temperature that preceded the work reported here.

As pointed out in Sec. II, irradiation at 720 K with 60 eV electrons was found to produce the best (1×2) structure as judged by peak-to-background ratio and peak width of the LEED spots. Under otherwise identical conditions, irradiation at 500 K caused only a strong increase of the background in the (1×1) LEED pattern with very weak and diffuse half order spots. Thus, not only at room temperature but even at 500 K the irradiated surface is considerably disordered. Subsequent annealing at temperatures up to 720 K decreased the background and somewhat sharpened the half order spots, but the resulting (1×2) structure was far inferior to that produced by irradiation at 720 K.

Apparently, at 720 K, the mobility of surface oxygen vacancies (including possibly produced deeper layer[25,26] bridging oxygen vacancies) is high enough to allow the surface to achieve quasiequilibrium at any moment during irradiation but not high enough to anneal out defect configurations produced at lower temperature, in particular, the disorder observed at room temperature as reported in Ref. 55. In view of the surface transport processes needed to achieve the minimum energy configuration, it is clear that the surface structure depends strongly on irradiation conditions, in particular, temperature.

*Present address: CELLS-ALBA Synchrotron Light Facility, C3 Campus Universitat Autónoma de Barcelona, 08193 Bellaterra, Barcelona, Spain.

[1] T. N. Rhodin, P. W. Palmberg, and C. J. Todd, in *Molecular Processes on Solid Surfaces* (McGraw-Hill, New York, 1969), p. 499.

[2] A. K. Green, J. Dancy, and E. Bauer, J. Vac. Sci. Technol. **7**, 159 (1970).

[3] J. A. Venables and J. H. Harding, J. Cryst. Growth **211**, 27 (2000); A. Green, E. Bauer, R. Peck, and J. Dancy, Krist. Tech. **5**, 345 (1970).

[4] J. A. Venables, L. Giordano, and J. H. Harding, J. Phys.: Condens. Matter **18**, S411 (2006).

[5] C. Ratsch and J. A. Venables, J. Vac. Sci. Technol. A **21**, S96 (2003).

[6] A. Locatelli, T. Pabisiak, A. Pavlovska, T. Mentes, L. Aballe, A. Kiejna, and E. Bauer, J. Phys.: Condens. Matter **19**, 082202 (2007).

[7] M. Haruta, T. Kobayashi, N. Yamada, and S. Iijima, J. Catal. **115**, 301 (1989).
[8] Q. Fu, H. Saltsburg, and M. Flytzani-Stephanopoulos, Science **301**, 935 (2003).
[9] M. Haruta, Chem. Rec. **3**, 75 (2003).
[10] U. Diebold, Surf. Sci. Rep. **48**, 53 (2003).
[11] K. F. McCarty and N. C. Bartelt, Phys. Rev. Lett. **90**, 046104 (2003); Surf. Sci. **527**, L203 (2003); **540**, 157 (2003).
[12] P. W. Murray, N. G. Condon, and G. Thornton, Phys. Rev. B **51**, 10989 (1995).
[13] H. Onishi and Y. Iwasawa, Surf. Sci. **313**, L783 (1994); Phys. Rev. Lett. **76**, 791 (1996).
[14] C. L. Pang, S. A. Haycock, H. Raza, P. W. Murray, G. Thornton, O. Gülseren, R. James, and D. W. Bullett, Phys. Rev. B **58**, 1586 (1998).
[15] R. A. Bennett, P. Stone, N. J. Price, and M. Bowker, Phys. Rev. Lett. **82**, 3831 (1999); R. A. Bennett, P. Stone, and M. Bowker, Faraday Discuss. **114**, 267 (1999).
[16] K. T. Park, M. H. Pan, V. Meunier, and E. W. Plummer, Phys. Rev. Lett. **96**, 226105 (2006).
[17] M. Blanco-Rey, J. Abad, C. Rogero, J. Méndez, M. F. López, J. A. Martín-Gago, and P. L. de Andrés, Phys. Rev. Lett. **96**, 055502 (2006).
[18] M. Blanco-Rey, J. Abad, C. Rogero, J. Méndez, M. F. López, E. Román, J. A. Martín-Gago, and P. L. de Andrés, Phys. Rev. B **75**, 081402(R) (2007).
[19] K. O. Ng and D. Vanderbilt, Phys. Rev. B **56**, 10544 (1997).
[20] M. D. Rasmussen, L. M. Molina, and B. Hammer, J. Chem. Phys. **120**, 988 (2004).
[21] E. Bauer and T. Schmidt, in *High Resolution Imaging and Spectroscopy of Materials* (Springer, Berlin, 2003), p. 363.
[22] A. Locatelli, L. Aballe, T. O. Mentes, M. Kiskinova, and E. Bauer, Surf. Interface Anal. **38**, 1554 (2006).
[23] M. L. Knotek and P. J. Feibelman, Phys. Rev. Lett. **40**, 964 (1978).
[24] Z.-J. Ding and R. Shimizu, Scanning **418**, 92 (1996).
[25] K. Hameeuw, G. Cantele, D. Ninno, F. Trani, and G. Iadonisi, Phys. Status Solidi A **203**, 2219 (2006).
[26] T. Pabisiak and A. Kiejna, Solid State Commun. (to be published).
[27] P. E. Blöchl, Phys. Rev. B **50**, 17953 (1994).
[28] G. Kresse and D. Joubert, Phys. Rev. B **59**, 1758 (1999).
[29] G. Kresse and J. Hafner, Phys. Rev. B **47**, 558 (1993); **49**, 14251 (1994).
[30] G. Kresse and J. Furthmüller, Phys. Rev. B **54**, 11169 (1996); Comput. Mater. Sci. **6**, 15 (1996).
[31] J. P. Perdew, K. Burke, and M. Ernzerhof, Phys. Rev. Lett. **77**, 3865 (1996).
[32] H. J. Monkhorst and J. D. Pack, Phys. Rev. B **13**, 5188 (1976).
[33] A. Kiejna, T. Pabisiak, and S. Gao, J. Phys.: Condens. Matter **18**, 4207 (2006).
[34] G. Cabailh, X. Torrelles, R. Lindsay, O. Bikondoa, I. Joumard, J. Zegenhagen, and G. Thornton, Phys. Rev. B **75**, 241403(R) (2007).
[35] E. Wahlström, N. Lopez, R. Schaub, P. Thostrup, A. Rønnau, C. Africh, E. Lægsgaard, J. K. Nørskov, and F. Besenbacher, Phys. Rev. Lett. **90**, 026101 (2003).
[36] K. P. Huber and G. Herzberg, *Constants of Diatomic Molecules* (Van Nostrand Reinhold, New York, 1979).
[37] P. H. Citrin, G. K. Wertheim, and Y. Baer, Phys. Rev. Lett. **41**, 1425 (1978).
[38] M. A. Henderson, Surf. Sci. **419**, 174 (1999).
[39] I. N. Remediakis, N. Lopez, and J. K. Nørskov, Appl. Catal., A **291**, 13 (2005).
[40] D. Matthey, J. G. Wang, S. Wendt, J. Matthiesen, R. Schaub, E. Lægsgaard, B. Hammer, and F. Besenbacher, Science **315**, 1692 (2007).
[41] X. Lai, T. P. S. Clair, M. Valden, and D. W. Goodman, Prog. Surf. Sci. **59**, 25 (1998).
[42] M. Valden, X. Lai, and D. W. Goodman, Science **281**, 1647 (1998).
[43] F. Cosandry and T. E. Madey, Surf. Rev. Lett. **8**, 73 (2001).
[44] C. E. J. Mitchell, A. Howard, M. Carney, and R. G. Egdell, Surf. Sci. **490**, 196 (2001).
[45] Y. Maeda, T. Fujitani, S. Tsubota, and M. Haruta, Surf. Sci. **562**, 1 (2004).
[46] N. Lopez and J. Nørskov, Surf. Sci. **515**, 175 (2002).
[47] L. M. Molina, M. D. Rasmussen, and B. Hammer, J. Chem. Phys. **120**, 7673 (2004).
[48] J. G. Wang and B. Hammer, Phys. Rev. Lett. **97**, 136107 (2006).
[49] T. Schmidt and E. Bauer, Phys. Rev. B **62**, 15815 (2000).
[50] G. Barcaro, A. Fortunelli, F. Nita, and R. Ferrando, Phys. Rev. Lett. **95**, 246103 (2005).
[51] C. Park, M. Kramer, and E. Bauer, Surf. Sci. **109**, L533 (1981).
[52] U. Stawinski and E. Bauer, Phys. Rev. B **47**, 12820 (1993).
[53] F. Golek and E. Bauer, Surf. Sci. **365**, 547 (1996).
[54] M. Szymonski, J. Kolodziej, Z. Postawa, P. Czuba, and P. Piatkowski, Surf. Sci. **48**, 83 (1995).
[55] C. L. Pang *et al.*, Nanotechnology **17**, 5397 (2006).